Shock Waves (2001) 10: 431–443

Shock Waves

Explosive dispersal of solid particles

F. Zhang[1], D.L. Frost[2], P.A. Thibault[3], S.B. Murray[1]

[1] Defence Research Establishment Suffield, PO Box 4000, Stn Main, Medicine Hat, Alberta T1A 8K6, Canada
[2] Mechanical Engineering, McGill University, Montreal, Quebec H3A 2K6, Canada
[3] Combustion Dynamics Ltd., 132 4th Avenue SE, Medicine Hat, Alberta T1A 8B5, Canada

Received 16 August 1999 / Accepted 26 June 2000

Abstract. The rapid dispersal of inert solid particles due to the detonation of a heterogeneous explosive, consisting of a packed bed of steel beads saturated with a liquid explosive, has been investigated experimentally and numerically. Detonation of the spherical charge generates a blast wave followed by a complex supersonic gas-solid flow in which, in some cases, the beads catch up to and penetrate the leading shock front. The interplay between the particle dynamics and the blast wave propagation was investigated experimentally as a function of the particle size (100–925 μm) and charge diameter (8.9–21.2 cm) with flash X-ray radiography and blast wave instrumentation. The flow topology during the dispersal process ranges from a dense granular flow to a dilute gas-solid flow. Difficulties in the modeling of the high-speed gas-solid flow are discussed, and a heuristic model for the equation of state for the solid flow is developed. This model is incorporated into the Eulerian two-phase fluid model of Baer and Nunziato (1986) and simulations are carried out. The results of this investigation indicate that the crossing of the particles through the shock front strongly depends on the charge geometry, the charge size and the material density of the particles. Moreover, there exists a particle size limit below which the particles cannot penetrate the shock for the range of charge sizes considered. Above this limit, the distance required for the particles to overtake the shock is not very sensitive to the particle size but remains sensitive to the particle material density. Overall, excellent agreement was observed between the experimental and computational results.

Key words: Explosion, Detonation, Blast wave, Heterogeneous explosive, Multiphase gas-solid flow

1 Introduction

When an explosive containing solid particles is detonated, a detonation wave will propagate in the heterogeneous material and compact the solid particles. The propagation of a detonation through such an explosive, consisting of a packed bed of solid spheres saturated with a liquid explosive, has been investigated experimentally by researchers including Kurbangalina (1969) and Lee et al. (1995a,b). They measured the detonation velocity and failure diameter as a function of the sensitivity of the explosive and the particle diameter. However, the dynamics of the subsequent particle dispersion process have yet to be investigated systematically.

If a heterogeneous explosive containing inert particles is detonated, when the detonation wave reaches the charge surface, a blast wave will be transmitted into the air. An expansion wave will also be reflected at the charge surface and the solid particles will be dispersed by the flow of the expanding explosion products. Important features in this dispersal process include the initial geometry (i.e., planar, cylindrical or spherical) of the charge and the concentration and velocity profiles of the dispersed solid particle cloud as a function of time. The question naturally arises as to whether or not the solid particles can cross the explosion products and penetrate the shock front. Very fine particles will rapidly equilibrate to the flow velocity of the combustion products whereas large particles will respond slowly due to their large inertia. Therefore, there will exist an intermediate range of particle sizes for which the inertia of the particles combined with the decay of the blast wave produces a "sling-shot" effect in which the particles catch up with and penetrate the combustion products contact surface and, in some cases, overtake the primary shock front. Lanovets et al. (1991) performed preliminary numerical simulations for spherical charges and reported that the solid particles can, for a certain range of particle size and density, cross the explosion products and overtake the primary shock front.

In this paper, we systematically describe our experimental and numerical investigation on the mechanism by which solid particles penetrate the shock front during the explosive dispersion process. The particles are assumed to be chemically inert and the investigation is performed over

Correspondence to: F. Zhang (e-mail: fzhang@dres.dnd.ca)

a range of charge geometry, charge size or mass, size and material density of the particles, and the volume fraction occupied by the particles. Some of the results can also be found in earlier reports (Zhang et al. 1997, 1999).

In the explosive dispersal process, the flow topology ranges from a granular flow during the propagation of the detonation within the charge to a dilute gas-solid flow at distances far from the source. Between these two extremes, there exists a dense gas-solid flow regime found in the early time of the explosion. In this transition regime, the particles interact mostly through random inelastic collisions which cause difficulties for current theories in describing constitutive equations of the solid flow without an interstitial gas. Consequently, uncertainties exist for the pressure and sound speed of the solid flow that are derived from these constitutive equations. These variables are of importance for making a reasonable prediction of the near-field supersonic flow. Direct experimental data of these variables in this regime are also not readily found in the open literature. In the present paper, problems associated with the pressure and sound speed used in the current solid flow models will first be discussed. Because of the lack of a sound theory and experimental data, a heuristic constitutive model for the solid flow is used to satisfy the sound speed asymptotic limits of both the solid and the dilute solid flow. This model is incorporated into the Eulerian two-fluid model of Baer and Nunziato (1986) and the numerical simulation results are then compared with the current experimental results.

2 Multiphase modeling issues

2.1 Frozen sound speed of the solid flow

A gas-solid two-phase flow may be considered to consist of a large number of solid particles immersed in a gas. In a gas-solid flow, the gas and solid particles are treated as two separate flows which are coupled through their interactions. The following discussion is focused on the solid flow without interstitial gas. Depending on the volume fraction, ϕ_s, occupied by the solid phase, a particular gas-solid flow topology can be classified either as a dilute gas-solid flow ($\phi_s < 0.01$), a dense gas-solid flow ($0.01 < \phi_s < \phi_{s,\text{packed}}$), or a granular flow ($\phi_s \geq \phi_{s,\text{packed}}$). In the limit of a very dilute gas-solid mixture in which the particles are discrete and far from each other, the probability of a particle-particle collision is very low and hence the interactions between the particles can be neglected. Consequently the pressure and the sound speed of the solid flow is negligible (Rudinger, 1980). At the other extreme limit of a granular flow, the particles are closely packed and forces are exerted on the individual particles by direct contact with the neighboring particles and by the gas in the pore spaces. The competition between these external forces and the stresses within the particle created by the compression and deformation forms the leading mechanism for the compaction of the granular material. Using continuum theory and the second law of thermodynamics, Baer and Nunziato (1986) developed a model for the rate-dependent dynamic compaction controlled by the mechanical nonequilibrium. Due to the large solid volume fraction, the pressure and sound speed of the solid flow are close to those of the solid itself.

Between the above two limits, there exists a regime where the particles mostly interact through random inelastic collisions. In this transition regime, the definitions of the pressure and sound speed of the high-speed solid flow have not been well established. In the continuum theory for granular flows, the density and pressure of the solid flow, ρ_p and p_p, are often assumed to be equal to the solid volume fraction, ϕ_s, times the material density and pressure, ρ_s and p_s, respectively (Baer and Nunziato, 1986; Powers et al., 1990):

$$\rho_p = \phi_s \rho_s \tag{1}$$

$$p_p = \phi_s p_s \; . \tag{2}$$

Here, the subscript p refers to the discrete solid flow and the subscript s refers to the solid. These definitions result in a phase-frozen sound speed for the solid flow, a_p, that equals the sound speed of the solid, a_s (Embid and Baer, 1992):

$$a_p^2 = \left(\frac{\partial p_p}{\partial \rho_p}\right)_{s_s,\phi_s} = \left(\frac{\partial p_s}{\partial \rho_s}\right)_{s_s,\phi_s} = a_s^2 \; . \tag{3}$$

The volume-averaging assumptions are appropriate for the granular flow when the solid volume fraction asymptotically approaches unity during the dynamic compaction. However, difficulties are encountered when these assumptions are used for the dense and dilute solid flows. For example, although the pressure of the solid flow approaches zero as the solid volume fraction approaches zero, the resultant sound speed of the solid flow always equals the sound speed of the solid regardless of how small the solid volume fraction becomes. This conclusion contradicts the common fact that the sound speed of the solid flow diminishes rapidly as the solid volume fraction approaches zero. Clearly, the sound speed in a flow of a dispersed solid is different from that of the solid due to the spaces between the particles. Though the partial pressure rule (2) has often been used in the classical theory of gas mixtures, distribution of the solid pressure into the surrounding space following rule (2) may physically be unrealizable.

A correct definition of the sound speed in the dense solid flow is crucial for describing compressible phenomena of the flow. However, the asymptote of the volume-averaged granular flow theory has not provided a satisfactory formulation base. Although a macroscopic particle system and a molecular system are analogous in many ways, the two systems have many fundamental differences. A careful study of these fundamental differences is necessary and may lead to a novel analysis of dissipative statistical mechanics. As the available computational power increases, the dissipative statistical mechanical analysis will be made easier through direct simulations of a large number of particles at the "microscopic" particle scale (Baer, 1997).

2.2 A heuristic model for the solid flow

Due to the lack of a sound theoretical basis for compressible dense solid flow, the transition regime will be addressed by estimating the pressure and sound speed of the particle system using a heuristic interpolation method. This is realized by applying a weighting function to the solid volume fraction between the solid limit and the dilute solid flow limit. This approximation may be expected to give reasonable results for problems in which the transition regime from a granular flow to a dilute solid flow occurs in a relatively short time. The heuristic model that must satisfy the sound speed asymptote for both the solid limit and the dilute solid flow limit is assumed to have the form:

$$\begin{aligned} p_p &= P(\rho_s\,,\,T_s\,,\,\phi_s)\;, \\ e_p &= E\,(\rho_s\,,\,T_s)\;, \end{aligned} \tag{4}$$

that satisfies

$$\begin{aligned} P(\rho_s\,,\,T_s\,,\,\phi_s) &\to p_s(\rho_s\,,\,T_s), \quad \text{as} \quad \phi_s \to 1\,, \\ P(\rho_s\,,\,T_s\,,\,\phi_s)/\rho_p &\to 0, \quad \text{as} \quad \phi_s \to 0 \;\&\; \rho_s \to \rho_{s0}\,, \end{aligned} \tag{5}$$

with $\rho_p = \phi_s \rho_s$. Here, the subscript 0 refers to the initial state and the variable T is the temperature. The variable e_p is the specific internal energy defined as the internal energy per mass of the solid flow, and therefore equals the specific internal energy of the solid, e_s. Defining the phase-frozen sound speed of a solid flow by

$$a_p^2 = \left(\frac{\partial p_p}{\partial \rho_p}\right)_{s_p,\phi_s} = \frac{1}{\phi_s}\left(\frac{\partial p_p}{\partial \rho_s}\right)_{e_p,\phi_s} + \frac{p_p}{\phi_s^2 \rho_s^2}\left(\frac{\partial p_p}{\partial e_p}\right)_{\rho_p,\phi_s} \tag{6}$$

where s_p denotes the specific entropy of the solid flow, the heuristic equation of state (4–5) must yield

$$\begin{aligned} a_p &\to a_s \quad \text{as} \quad \phi_s \to 1\,, \\ a_p &\to 0 \quad \text{as} \quad \phi_s \to 0\,. \end{aligned} \tag{7}$$

As an example, we consider the Mie-Gruneisen equation of state for a solid under high pressure

$$p_s = p_H(\rho_s) + \rho_s \Gamma(\rho_s)[e_s - e_H(\rho_s)]\;, \tag{8}$$

where the subscript H denotes values on the Hugoniot curve and Γ is the Grüneisen gamma. This equation of state extends the shock wave data to regions off the shock Hugoniot. From (4–7) a heuristic equation of state for a solid flow can be formally written as

$$p_p = g_1(\phi_s) p_H(\rho_s) + g_2(\phi_s)\rho_s \Gamma(\rho_s)\,[e_s - e_H(\rho_s)] \tag{9}$$

with

$$\begin{aligned} g_1(\phi_s) = O(\phi_s), \qquad & g_2(\phi_s) = O(\phi_s^n) \\ \text{with} \quad & n > 1\,. \end{aligned} \tag{10}$$

Here, p_H equals the value on the solid Hugoniot when $\rho_s/\rho_{s0} \geq 0$ and is assumed to be null when $\rho_s/\rho_{s0} < 0$. A heuristic equation of state for a solid flow based on the Sheffield equation for solid (Sheffield et al., 1977) can be formally written as

$$\begin{aligned} p_p = g_1(\phi_s)\frac{K}{N}\left[\left(\frac{\rho_s}{\rho_{s0}}\right)^N - 1\right] \\ + g_2(\phi_s)\rho_s \Gamma_0 c_{vs}(T_s - T_{s0}) \end{aligned} \tag{11}$$

where $g_1(\phi_s)$ and $g_2(\phi_s)$ satisfy Eq. (10). The parameter K equals the bulk compression modulus when $\rho_s/\rho_{s0} \geq 0$ and is assumed to be null when $\rho_s/\rho_{s0} < 0$. Generally speaking, the heuristic approach used here is essentially an empirical macroscopic approach. For simplicity, $g_1 = \phi_s$ and $g_2 = \phi_s^2$ are assumed.

2.3 Governing equations

Because of the large solid volume fractions and supersonic flows involved, we choose an Eulerian two-fluid model in which a control volume is comprised of the sum of the separate volumes occupied by the solid and gas phase. Viscosity and conductivity associated with molecular transport in the gas and with interparticle kinetic-collisional transport as well as gravity effects were not considered. The Eulerian two-fluid model consists of three parts: Eulerian conservation equations, constitutive equations for materials, and interphase interaction functions. To solve a compressible gas-solid flow in which the mixture changes from a granular material to a highly dilute gas-particle suspension, we have focused on the solid phase constitutive equations from which the pressure and sound speed can be obtained. In deriving the governing equations for an Eulerian two-fluid model, the theory of Baer and Nunziato (1986) for granular flows is adopted and extended for the dilute solid flow. The resultant governing equations for the solid flow are:

number density:

$$\frac{\partial n_p}{\partial t} + \frac{\partial}{\partial x_i}\left(n_p u_{pi}\right) = N_p\;, \tag{12}$$

continuity equation:

$$\frac{\partial \rho_p}{\partial t} + \frac{\partial}{\partial x_i}\left(\rho_p u_{pi}\right) = J_p\;, \tag{13}$$

compaction:

$$\frac{d\phi_s}{dt} = \Phi_p + \phi_s \frac{J_p}{\rho_p}\;, \tag{14}$$

momentum equation:

$$\rho_p \frac{du_{pi}}{dt} = -\frac{\partial\, p_p}{\partial x_i} + f_{pi}\;, \tag{15}$$

energy equation:

$$\rho_p \frac{de_p}{dt} = -p_p \frac{\partial u_{pi}}{\partial x_i} + Q_p - \left(\frac{p_p}{\phi_s} - \beta_p\right)\Phi_p\;. \tag{16}$$

The first equation is the particle number equation where n_p stands for the number of particles per unit volume and u_{pi} is the velocity component in x_i direction. The source term on the RHS, N_p, represents the rate of change of the number of particles due to particle agglomeration or breakup. In the continuity equation (13), the RHS source term, J_p, represents the rate of mass change between the solid and the gas due to, for instance, evaporation or combustion. In this paper, we limit ourselves to a solid flow whose mass and particle number are conserved, i.e., $N_p = J_p = 0$. In Eq. (14), the first source term, Φ_p, on the RHS describes the dynamic compaction of the granular material using the Baer-Nunziato model, in which the rate of change of the solid volume fraction is determined by the mechanical nonequilibrium between the solid pressure, gas pressure, and a bed configuration stress β_s (Baer and Nunziato 1986):

$$\Phi_p = \frac{(1-\phi_s)[p_s - p_g - \beta_s(\phi_s)]/\beta_{s,\,ref}}{\tau_c} \,, \tag{17}$$

with the saturation confinement,

$$\phi_g + \phi_s = 1 \tag{18}$$

where ϕ_g is the volume fraction of gas. The configuration stress represents the resistance against a change in the packing of the particle bed. The dependence of the configuration stress on the solid volume fraction is determined by the quasi-static compaction test, and thus reflects the effects of compression and shear deformation of particles as well as interparticle frictional effects. The process of equilibration between the two phases is controlled by the compaction time scale, τ_c. The second term on the RHS of the compaction Eq. (14) describes the solid volume depletion due to mass transfer into the gas.

The conservation of momentum (15) is described by Newton's second law. The rate of change of momentum is caused by the pressure gradient of the solid flow and the rate of momentum transfer between the solid flow and the gas. Forces that are exerted on the solid particles which contribute to interphase momentum transfer include drag, forces due to the gas pressure gradient and added mass, and the Basset history force (Rudinger 1980). Among these forces, the drag due to the relative velocity between the two phases is dominant and the other forces can also incorporated into an effective drag coefficient. The drag can be formally expressed by:

$$f_{pi} = \frac{\rho_p(u_{gi} - u_{pi})}{\tau_u} \tag{19}$$

with

$$\tau_u = \tau_u(\rho_g, \rho_s, d_s, \phi_s, \mathrm{Re}, M) \,, \tag{20}$$

where Re and M are the Reynolds number and flow Mach number defined by the relative velocity between the solid flow and gas flow. The time scale τ_u controls the relaxation process of the momentum nonequilibrium between the solid particles and the gas.

The last conservation Eq. (16) is the first law of thermodynamics for the internal energy. The first two terms on the RHS represent the work done by the pressure of the solid flow and the energy transferred between the solid and gas phase, respectively. For the dispersal problem, the rate of energy transfer, Q_p, is simply represented by the rate of heat transfer due to the temperature difference between the solid particles and the gas:

$$Q_p = \frac{\rho_p c_{vp}(T_g - T_s)}{\tau_T} \tag{21}$$

with

$$\tau_T = \tau_T(T_g, \rho_s, d_s, \phi_s, \mathrm{Re}, M, \mathrm{Pr}) \tag{22}$$

where Pr is the prandtl number. The time scale τ_T controls the relaxation process of the thermal nonequilibrium between the phases. The last term on the RHS of (16) is the dissipation work done in compacting the granular material. The energy dissipated during compaction goes to increase the internal energy of the gas.

The governing equations for the gas flow are summarized below:

$$\frac{\partial \phi_g \rho_g}{\partial t} + \frac{\partial}{\partial x_i}(\phi_g \rho_g u_{gi}) = -J_p \,, \tag{23}$$

$$\phi_g \rho_g \frac{d\, u_{gi}}{dt} = -\frac{\partial}{\partial x_i}(\phi_g p_g) - f_{pi} - J_p(u_{pi} - u_{gi}) \,, \tag{24}$$

$$\begin{aligned} \phi_g \rho_g \frac{de_g}{dt} = & -\phi_g p_g \frac{\partial u_{gi}}{\partial x} + \phi_g \rho_g q_g - Q_p \\ & + \left(\frac{p_p}{\phi_s} - \beta_p\right)\Phi_p - f_{pi}(u_{pi} - u_{gi}) \\ & - J_p\left[(e_p - e_g) + \frac{1}{2}(u_p - u_g)^2\right] \,, \end{aligned} \tag{25}$$

$$\frac{dY_{gj}}{dt} = w_{gj} \,, \quad j = 1 \quad \text{to} \quad s \,. \tag{26}$$

Here, u_{gi} is the velocity component for the gas flow in x_i direction. In Eq. (25) and (26), the source term q_g represents the heat release rate of the gas phase reactions and w_{gi} is the rate of mass change for the i-th gas species. If the gas phase is assumed to be chemically non-reactive, then $q_g = w_{gi} = 0$.

The governing equations derived for the gas-solid flows, together with gas equations of state and the heuristic model for the solid particle system provide closure for the compressible gas-solid flow. The JWL equation of state was used for the explosion products and the van der Waals' equation of state for the air. The heuristic EOS model (11) was used for the solid particle system. With the frozen sound speed derived from the heuristic model for the solid flow, it is possible to solve the problems ranging from a granular material to a dilute gas-solid mixture. The conservation equation system for the solid flow is hyperbolic and its characteristic speeds are $u_{pi} - a_p$, u_{pi}, and

$u_{pi} + a_p$. For a granular flow and for the transition regime from the granular material to a dilute gas-solid mixture, an acoustic wave or a shock wave may be present in the solid flow. However, the frozen sound speed and therefore the wave structure also depend on the solid volume fraction which decays during the dispersal process. For the dilute solid flow with a negligible solid volume fraction, the frozen sound speed disappears and the conservation equations degenerate into a parabolic form with a characteristic speed of u_{pi}. Only a dissipative wave structure can be observed in this case.

The challenge for a numerical solver for such a multi-regime gas-solid flow is to handle the solid phase with a frozen sound speed spectrum ranging from 0 to 10^3 m/s. The stiffness arises from the large difference in the phase material densities and from the multiple time scales caused by the interphase interaction processes. A second-order Godunov-type explicit scheme including Roe's Riemann solver is used to solve the gas flow. To deal with real gas effects due to high pressure and density, a conservation equation is included for the thermodynamic function (Colella and Glaz, 1985)

$$\gamma_g = \frac{p_g}{\rho_g e_g} + 1 \,. \tag{27}$$

Considering the solid flow, to ensure continuity in the solution during the solver switching between the hyperbolic and parabolic equation systems, we choose a McCormack predictor-corrector scheme with a fourth-order Flux Corrected Transport (FCT) technique. The source terms are treated using the time-splitting technique. This model is then implemented in the IFSAS code of Combustion Dynamics Limited (Zhang et al., 1996).

3 Experimental

Experiments were carried out using spherical charges consisting of packed beds of inert spherical steel particles saturated with nitromethane sensitized with 10% by weight triethylamine. Spherical glass charge casings with diameters of 8.9 and 11.8 cm were prepared by removing the filaments from standard globe light bulbs. Large charges with a diameter of 21.2 cm utilized a standard 5 liter spherical boiling flask to contain the heterogeneous explosive. These charge diameters are far beyond the critical tube diameter for the explosive which ranges between 1.5 and 2.5 cm (Lee et al. 1995b). The particle size was varied over an order of magnitude (from about 100 μm to 925 μm). Most of the trials were carried out with spherical steel particles obtained from Draiswerke Inc. (Mahwah, NJ) which were sieved to one of the following 4 different sizes: 98±8 μm, 275±25 μm, 463±38 μm, or 925±75 μm. For particle sizes of 275 μm and larger, the solid mass fraction of the packed steel particles in the charge was consistently measured to be 92%±1% (corresponding to a solid volume fraction of 62%) from one trial to the next. For steel particles with a nominal size of 100 μm or less, the solid packing density was less and the solid mass fraction of a charge was typically 83%±1%. The mass of liquid explosive was varied over an order of magnitude (from about 180 g to 430 g to 2360 g for charge diameters from 8.9 cm to 11.8 cm to 21.2 cm, respectively). The spherical charges were centrally initiated with a small charge (typically 7 g) of DM-12 explosive (comprised of 86% PETN, 13% oil and grease and 1% calcium sterate). This burster charge was placed in a small glass bulb (5 ml volume) that was blown on the end of a narrow (8 mm id) glass tube. The glass bulb was held in place at the center of the charge by epoxying it to a wooden disk at the mouth of the spherical charge. Prior to a trial, the burster charge was placed in the bulb, and the sphere was filled with particles and then sensitized NM. Finally, the spherical charge was placed at the test site and a Reynold's bridgewire detonator was inserted into the glass tube to the center of the charge (an RP-2 minidetonator was used with the smaller spheres and an RP-83 detonator with the 5 liter spheres) and then the tube was stemmed with particles. The first radiograph shown in Fig. 2, taken prior to a trial, shows the initial charge with the glass tube protruding from the top of the sphere.

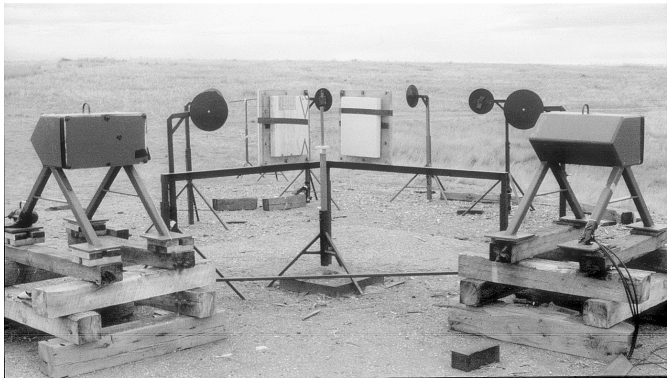

Fig. 1. Experimental setup. Two flash X-Ray pulsers are contained within the casings visible at each side of the photograph. The charge (in this case a cylinder) is mounted on a wooden post held by a stand in the middle of the photograph. Behind the charge are two plywood X-Ray cassettes, protected with a layer of Styrofoam

The experimental setup shown in Fig. 1 used a centrally located wood post with a plastic coupling to support the charge. The diagnostics included time-of-arrival contact gauges (consisting of two strips of metal foil sandwiching a mylar strip containing holes at regular intervals) flush-mounted on two steel beams in radial directions (not visible in Fig. 1), and six PCB piezoelectric pressure transducers flush-mounted in sharp-edged steel disks (30 cm dia) with their surfaces parallel to the radial direction. These gauges were used to determine the shock front trajectory and the pressure history. The pressure transducers used (PCB Models 113A24 and 111A26) have a risetime of about 1 μs. Signals were recorded with a PC-based data acquisition system (Gagescope, 25 MHz bandwidth) with a sampling rate per channel of 25 Msamples/s.

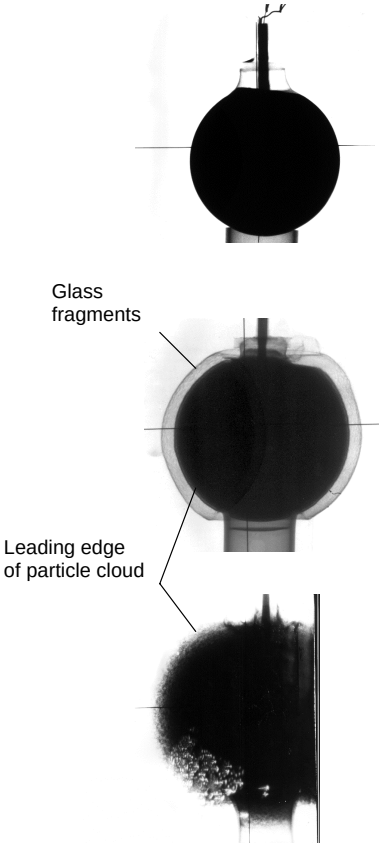

Fig. 2. X-Ray radiographs of the particle dispersal process with an 11.8 cm diameter spherical charge consisting of packed beds of 275 μm steel particles (4,400 g) saturated with sensitized nitromethane (434 g). *Upper photograph:* $t = 0\,\mu s$, *middle:* $t = 43\,\mu s$, *lower:* $t = 102\,\mu s$ after firing of the bridgewire detonator. The bright lines visible in the lower left part of the charge at $t = 102\,\mu s$ are produced by the discharge of static electrical charges that build up between the X-Ray film and screen during the interaction with the blast wave from the explosion

The charge and the pressure gauges were located 1.5 m above the ground so that the reflected blast wave from the ground did not reach the gauge located furthest from the charge until the primary blast wave at that location had decayed to atmospheric pressure. The particle dispersal process and the particle front trajectory were tracked using two 150 kV flash X-ray pulsers. The two flash X-ray pulsers are contained within the casings visible at each side of the photograph. The X-Ray film/screen combination was mounted within plywood cassettes and placed on break-away stands typically 50 cm from the charge. The charge-pulser distance was about 2 m, so that the magnification factor on the X-Ray film was 1.25. The cassettes were thrown a considerable distance by the blast wave, but survived intact for charges containing less than 500 g of explosive. A Styrofoam sheet was placed in front of each cassette to protect the front Lucite face of the cassette from particle impacts.

Figure 2 provides a series of X-ray radiographs illustrating the particle dispersal process for an 11.8 cm diameter spherical charge. The charge consists of packed beds of 275 μm steel particles (4400 g) saturated with sensitized nitromethane (434 g). The first picture shows the charge prior to the detonation of the burster charge. In the second radiograph, taken 43 μs after the detonation has been initiated, the detonation in the explosive has reached the charge surface and transmitted a spherical blast wave into the air. At this time, the glass bulb, which provides weak confinement for the heterogeneous explosive, has been shattered. The gray region surrounding the charge corresponds to the cloud of fine glass fragments that are carried radially outwards by the expanding combustion products. Later, at 102 μs, the glass fragments are no longer visible, but a gradient in the particle concentration is clearly formed at the edge of the steel particle cloud. Note that the bright lines visible in the lower left part of the charge at $t = 102\,\mu s$ are produced by the discharge of static electrical charges that build up between the X-ray film and X-ray screen during the interaction with the blast wave from the explosion. For particles with sizes greater than or equal to 275 μm, individual particles are clearly visible on the radiographs. However, for 100 μm particles, the particle front can only be discerned at very early times. The position of the particle front is measured at the edge of the particle cloud. To determine the position of the leading edge of the particle cloud, the diameter of the particle cloud visible on the radiographs was determined using lines oriented at three different angles to the horizontal: 0°, and ±45°. Although the surface of the gaseous combustion products exhibits some perturbations (see Fig. 3), the particle cloud is remarkably spherically symmetric, except near the top and bottom of the charge. As a result, the value of the particle cloud diameter for the three different angles typically agreed within 2%. The particle dispersal was also monitored using high-speed framing photography (with a framing rate of 4,000 frames/s) as shown in Fig. 3 which shows the detonation of a 21.2 cm diameter (5 liter) spherical charge filled with about 26 kg of 463 μm steel beads and about 2,400 g of sensitized nitromethane. The particles cannot be discerned in the still photographs, but the approximately spherical cloud of combustion products has fine-scale perturbations on the surface. The bright flash visible at the top of the charge in the third frame (0.25 ms) is probably due to the detonation of a small layer of liquid nitromethane that was present above the saturated particle bed. The two large circular objects visible in the photographs are concrete cylinders located about 40 m behind the charge, and are not related to the present tests. Several pressure transducer stands are also visible to either side of the charge. No radiographs were obtained with the 21.2 cm charges since the X-ray cassettes could not survive the impact of the blast wave.

Due to the explosive expansion of the gaseous detonation products (with or without solid particles), the contact surface between the detonation products and the surrounding air is subject to the Rayleigh-Taylor instability. The perturbations on the surface of the detonation prod-

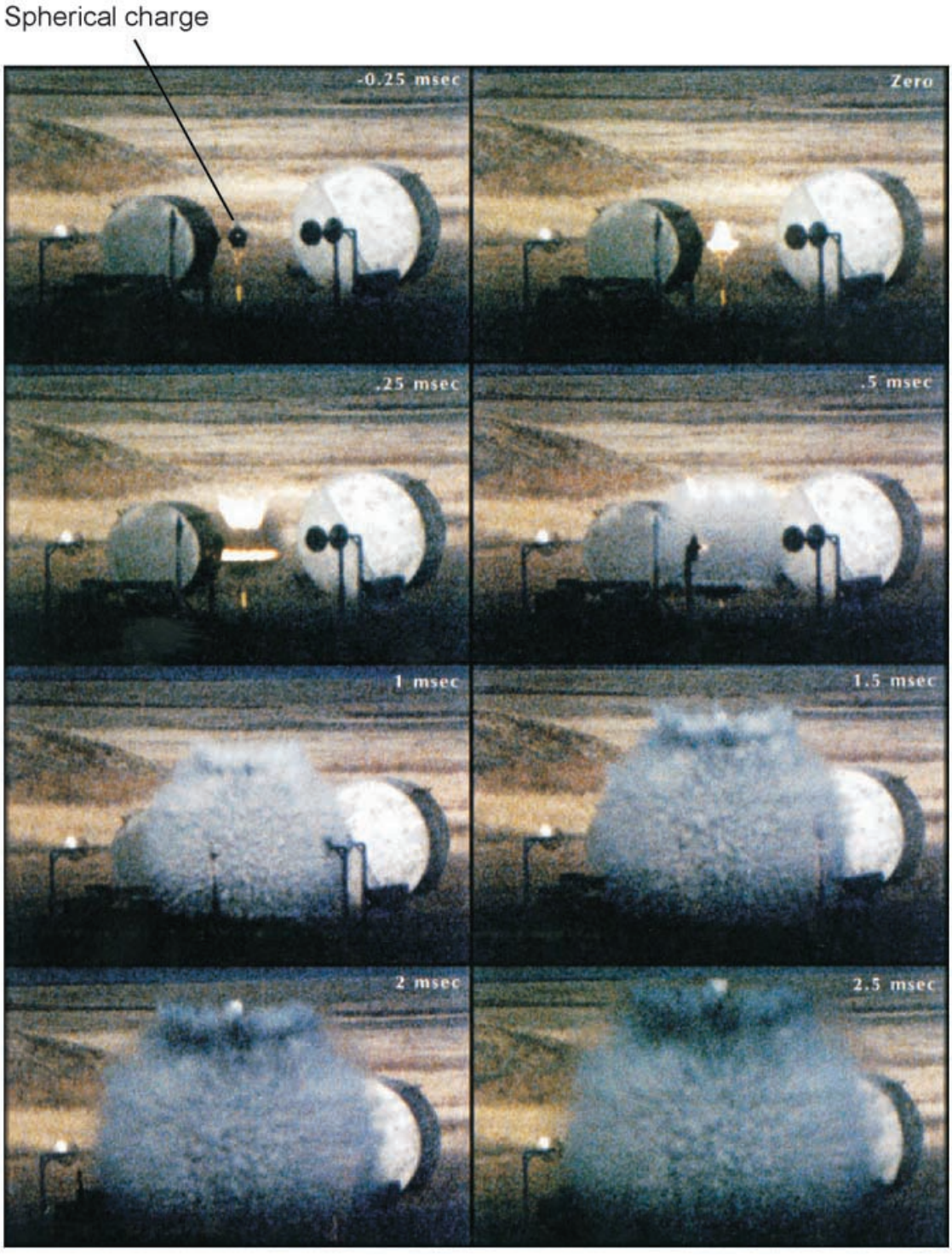

Fig. 3. High-speed framing photographs showing the expansion of the combustion products during the explosion of a 5 liter spherical (21.2 cm dia) charge consisting of a packed bed of 463 μm steel spheres saturated with sensitized nitromethane. The two large concrete cylinders visible in the photographs are located 40 m behind the charge and are unrelated to the present tests. Several pressure transducer stands are also visible in the photographs

ucts front evident in the high-speed photographs (Fig. 3) are associated with the formation of jets and random turbulent eddies. However, regardless of the instability of the detonation products contact surface, the particle cloud appears remarkably spherically symmetric. The spherical symmetry of the particle cloud suggests that the acceleration of the particles at the front of the packed bed occurs during the very initial stage of the dispersal process for the particle density and diameters studied. The instability of the detonation products front requires some time to develop to a significant magnitude; before that time the particles may already have moved out of the detonation products into the surrounding air. Although the turbulent perturbations around the particles can influence the particle motion, this effect will not be significant for particles with sufficiently large inertia and moving at a highly supersonic velocity. Hence, in the following discussion and analysis, the instability and turbulence perturbations are not included and the driving forces of the initial acceleration of the particles will be further examined.

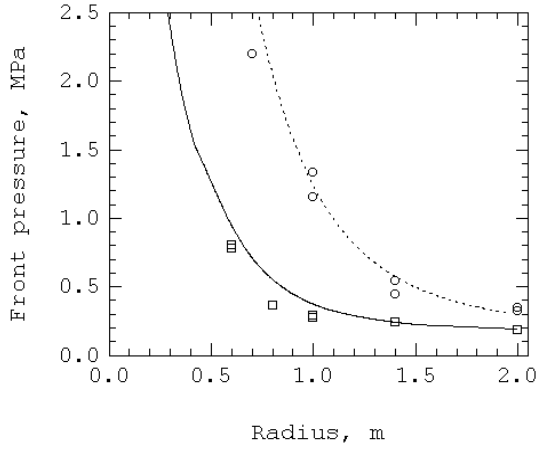

Fig. 4. Comparison of shock front overpressures for an 11.8 cm spherical charge with and without steel particles. Homogeneous charge contains 1,080 g of NM + 10% TEA whereas heterogeneous charge contains 430 g NM + 10% TEA with about 4,300 g of 463 μm steel beads. ○: Experiments with NM; □: experiments with NM/Fe; . . . . . .: simulation with NM; ___: simulation with NM/Fe

4 Results and discussion

4.1 Effect of inert particles on blast wave trajectory

In all the figures of this paper, symbols represent experimental results and lines correspond to the numerical simulations. In the numerical simulations, the trajectory of the front of the solid particle flow is tracked at a concentration level of $\rho_p = 1\,\mathrm{mg/m^3}$. A constant volume explosion process was assumed initially with the initial dimensions of the explosion products equal to the physical dimensions of the charge. Moreover, the weak confinement provided by the glass bulb was neglected. To set the initial conditions for the calculations, a constant volume explosion pressure of 4.5 GPa was chosen to fit the far-field pressure decay for the homogeneous charge, as shown in Fig. 4. This value is very close to the constant volume explosion pressure of 4.3 GPa predicted by the equilibrium code Cheetah (Fried et al., 1998) for NM + 10% TEA. The same initial pressure of the explosion products was used in all the subsequent numerical calculations presented. From Fig. 4, the simulation predicts the experimental overpressure for the heterogeneous charge well in the far field, but overpredicts the pressure in the near field. However, it should be noted that with the initial explosion pressure chosen for the calculations, the overpressure for a homogeneous nitromethane charge is also overpredicted in the near field.

Figure 5 compares the trajectories of the shock front and the explosion products contact surface for the explosion of charges with and without inert solid particles. The charge diameter in both cases is 11.8 cm. The homogeneous charge contained 1,080 g of nitromethane sensitized with 10% triethylamine whereas the heterogeneous charge contained 430 g NM + 10% TEA with about 4,300 g of 463 μm steel beads. Due to the momentum and energy loss from the gas to the particles, the addition of the particles reduces the propagation velocity of the shock front

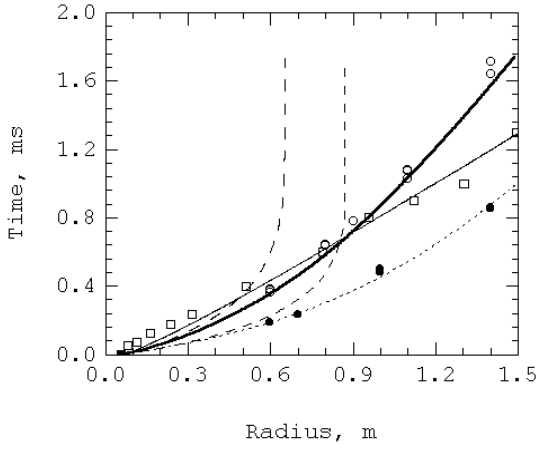

Fig. 5. Comparison of trajectories for the detonation of 11.8 cm spherical charges with and without steel particles. ●: Experimental shock front of NM; ○: experimental shock front of NM/Fe; □: experimental particle cloud front; . . . . . .: numerical shock front with NM; thick lines: numerical shock front with NM/Fe; thin line: numerical particle cloud front; dashed line: explosion products front, for NM (to the right) and for NM/Fe (to the left)

and the explosion products contact surface, thus resulting in a reduction of the shock pressure (see Fig. 4). The decay of the shock velocity and pressure indicates that the classic self-similar blast wave theory of Taylor and Sedov is not valid due to the extra scales introduced by the particles. While this paper focuses on the dispersal of solid particles, the effects of solid particles on the decay of the blast wave overpressure and impulse is described more fully in Frost et al. (1999). The trajectory of the

leading edge of the particle cloud, as determined directly from X-Ray radiographs, is shown in Fig. 5, together with the blast wave trajectory. The particles rapidly accelerate within about 10–20 cm to a terminal velocity between 1 and 2 km/s. The particle velocity is roughly constant until the particles overtake the blast wave, which occurs at a time of about 0.60 ms and at a shock front position of approximately 0.9 m. As the particles move ahead into the quiescent air, they decelerate due to the aerodynamic drag, and the blast wave will eventually catch up again with the particle front.

Since the solid particles at the front of the cloud are rapidly accelerated within a radius of one to two charge diameters to a terminal speed, the driving force for the particle motion is attributed largely to near-field effects. When the charge is detonated, a detonation wave propagates in the heterogeneous material and the solid particles are compacted by the high pressure of the explosion product gases. The solid particles reach the gas pressure within a compaction time scale which is proportional to the particle diameter divided by the solid sound speed. Hence, as the detonation wave reaches the charge surface, a large pressure gradient is immediately generated at the front of the packed bed of particles. This large solid pressure gradient results in an expansion wave into the solid particles and causes a large initial acceleration of the frontal particles. On the other hand, when the detonation wave reaches the charge surface, a rarefaction wave is reflected and causes the rapid acceleration of the explosion products. Consequently, the large velocity difference between the explosion products and the solid particles generates a drag which further accelerate the solid particles within the time scale of the momentum relaxation between the particles and the gas. The drag may also be enhanced by the interactions arising from the very dense particle system in the near field. The pressure gradient of the solid particles and the drag are the dominant driving forces causing the acceleration of the frontal particles in the near field. Figure 6 shows numerical simulation results with the drag and the pressure gradient of the solid particles for the 11.8 cm spherical charge, which consists of packed beds of 463 μm steel particles saturated with sensitized nitromethane. With the drag and the pressure gradient of the solid particles, the frontal particles cross the shock front at a much smaller distance than that with the drag alone. Further numerical simulations also indicated that other forces such as the pressure gradient within the gas, the Basset history force and the force due to accelerated gas near the particle surface (so-called added-mass effect) are less important. Therefore, all the numerical results of this paper were obtained using the drag and the pressure gradient of the solid particles as the driving forces for the particle motion.

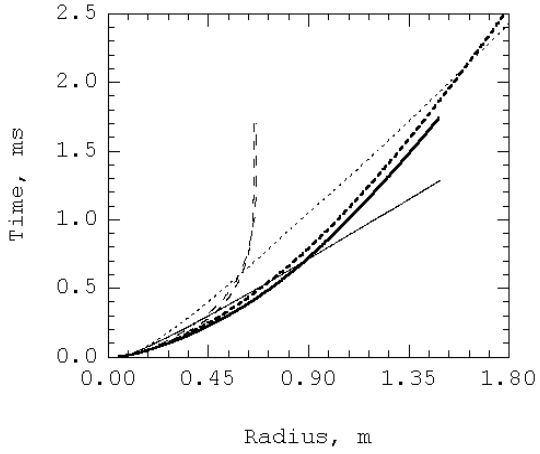

Fig. 6. Effect of particle driving forces on shock and particle trajectories for an 11.8 cm spherical charge consisting of packed beds of 463 μm steel particles saturated with sensitized nitromethane. ■■■: Numerical shock front with drag; .....: numerical particle cloud front with drag; thick line: numerical shock front with drag and pressure gradient of particles; thin line: numerical particle cloud front with drag and pressure gradient of particles; dashed line: explosion products front

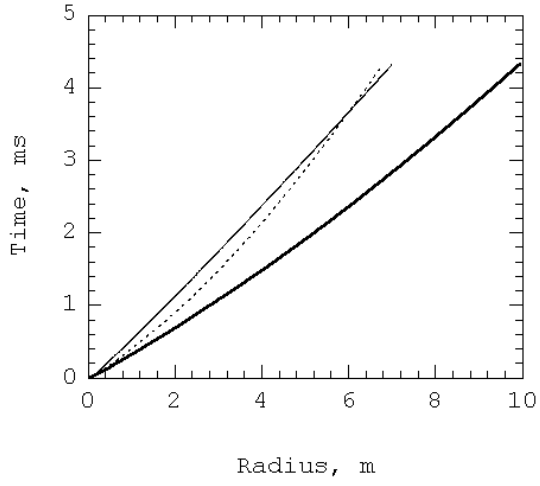

Fig. 7. Numerical trajectories for an 11.8 cm long charge with laterally rigid confinement resulting in a planar wave in the longitudinal direction. The charge consists of a packed bed of 463 μm steel particles saturated with sensitized nitromethane. Thick line: Shock front; thin line: front of particle cloud; dotted line: explosion products front

4.2 Effects of charge geometry

The penetration of solid particles through the shock front is mainly dependent on the choice of the charge geometry and the particle inertia. The role of the charge geometry is displayed in Figs. 7 and 8 in which the charge length scale and the steel particle diameter are fixed at 11.8 cm and 463 μm, respectively. For a charge configuration causing a planar shock wave, particles are unlikely to overtake the shock front due to the slow decay of the shock front caused by the Taylor expansion alone (see Fig. 7). If the charge configuration results in a diverging shock wave, the frontal curvature will cause a rapid deceleration of the shock front. Consequently, penetration of the

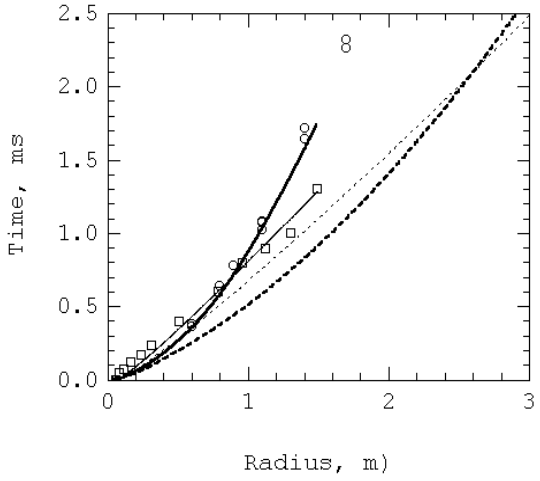

Fig. 8. Comparison of trajectories for cylindrical and spherical charges. In each case, the charge is 11.8 cm in diameter and consists of packed beds of 463 μm steel particles saturated with sensitized nitromethane. ○: Experimental shock front for the spherical case; □: experimental particle cloud front for the spherical case; thick line: numerical shock front for the spherical case; thin line: numerical particle cloud front for the spherical case; ■■■: numerical shock front for the cylindrical case; . . .. . .: numerical particle cloud front for the cylindrical case

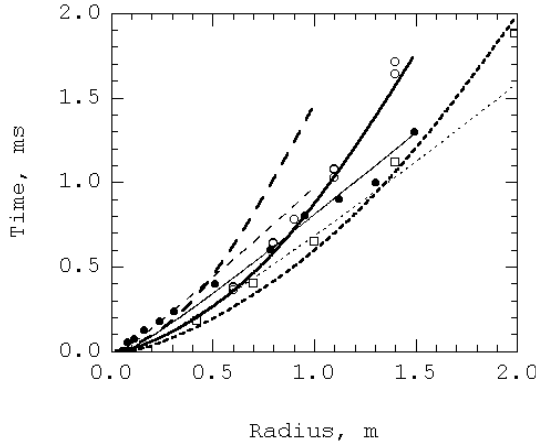

Fig. 9. Influence of charge diameter on trajectories. The spherical charge consists of a packed bed of 463 μm steel particles saturated with sensitized nitromethane. □: Experimental shock front for 21.2 cm charge diameter; ○: experimental shock front for 11.8 cm charge diameter; ●: experimental particle cloud front for 11.8 cm charge diameter; ■■■: numerical shock front for 21.2 cm charge diameter; dotted line: numerical particle cloud front for 21.2 cm charge diameter; thick line: numerical shock front for 11.8 cm charge diameter; thin line: numerical particle cloud front for 11.8 cm charge diameter; thick dashed line: numerical shock front for 6 cm charge diameter; thin dashed line: numerical particle cloud front for 6 cm charge diameter

particles through the shock wave becomes possible with a certain choice of charge mass and particle inertia. If the "overtaking distance" corresponds to the radius at which the frontal particles cross the shock front, Fig. 8 shows that the overtaking distance for a spherical shock wave is smaller than that for a cylindrical shock wave by a factor of three.

For spherical charges, increasing the charge diameter results in an increase in the overtaking distance. Figure 9 gives the results for charge diameters ranging from 6 to 21.2 cm with steel particles of 463 μm. The overtaking distance is increased by a factor of three when the charge diameter is increased from 6 cm to 21.2 cm. In other words, the overtaking distance is approximately proportional to the charge diameter, or to the charge explosive mass taken to the 1/3 power. This prediction is also observed in the experiments for charges of 8.9 cm and 11.8 cm in diameter. The overtaking time, which is proportional to the overtaking distance, is about 0.45 ms for the 8.9 cm charge and about 0.6 ms for the 11.8 cm charge, i.e., increasing the charge diameter by 33% increases the overtaking time by the same proportion.

4.3 Effects of particle inertia

For a given charge geometry, the overtaking distance depends on the solid particle inertia including its size and material density. The influence of the particle diameter on the overtaking distance is shown in Figs. 10 and 11 for steel particles and a spherical charge diameter of 11.8 cm.

For a particle diameter beyond a certain value, the trajectory of the particle front is almost a straight line and no significant change occurs in the trajectories of the shock front, the particle front and the explosion products front. This fact can be seen in Fig. 10 where the particle diameter varies from 275 μm to 925 μm and the overtaking distance is not changed significantly. From the momentum equation of the solid flow (15) and the analysis of the influence of various forces on the particle motion in Sect. 4.1, the acceleration of the particles is mainly caused by the pressure gradient of the solid flow and the drag. The pressure gradient of the solid flow is independent of the particle size based on the pressure Eq. (11). The magnitude of the drag is controlled by the time scale, τ_u, of the momentum relaxation between the two phases shown in Eq. (19), in which τ_u is proportional to the square of the particle diameter. Hence, the insensitivity to the particle size of the motion of large particles is the result of the smaller influence of the drag on the particle acceleration, because the momentum relaxation time scale is larger than the time scale of the overtaking process. Therefore, the initial acceleration of the large particles is dominated by the pressure gradient of the solid flow at the front of the packed bed of particles. After the initial acceleration, the frontal pressure gradient of the solid flow is reduced rapidly due to the decrease in the solid volume. Therefore, the acceleration is reduced rapidly and the motion of the frontal particles is then dominated by inertia and they move at a roughly constant velocity.

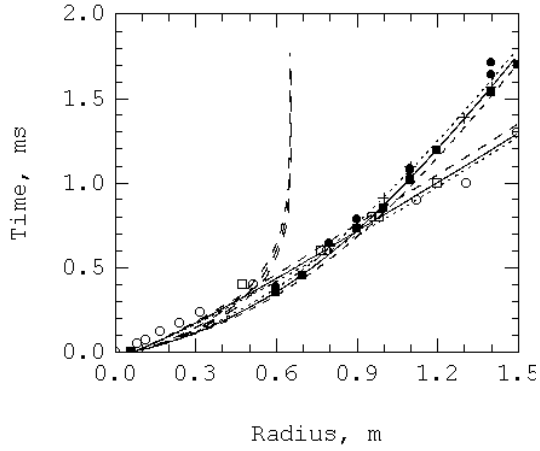

Fig. 10. Influence of particle diameter on trajectories (275–925 μm). The spherical charge is 11.8 cm in diameter and consists of packed beds of steel particles saturated with sensitized nitromethane. ■: Experimental shock front with 925 μm particles; •: experimental shock front with 463 μm particles; +: experimental shock front with 275 μm particles; □: experimental 925 μm particle cloud front; ○: experimental 463 μm particle cloud front; thin dashed line: simulation with 925 μm particles, curved line for shock front and straight line for particle cloud front; ___: simulation with 463 μm particles, curved line for shock front and straight line for particle cloud front; . . . . . .: simulation with 275 μm particles, curved line for shock front and straight line for particle cloud front; thick dashed line: numerical explosion products fronts for 275–925 μm, merged at about 0.65 m

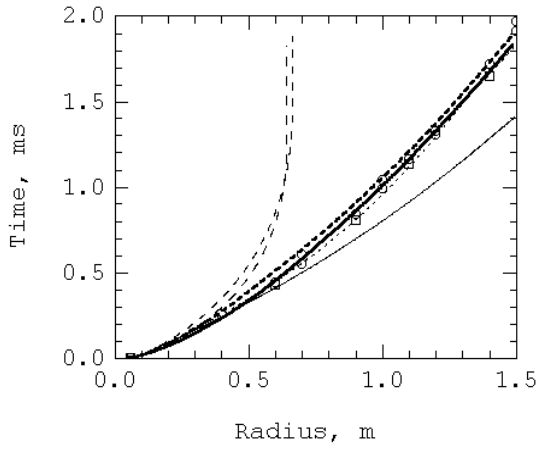

Fig. 11. Influence of particle diameter on trajectories (50–100 μm). The spherical charge is 11.8 μm in diameter and consists of a packed bed of steel particles saturated with sensitized nitromethane. ○: Experimental shock front with 100 μm particles; □: experimental shock front with 50 μm; thick line: numerical shock front with 100 μm particles; thin line: numerical 100 μm particle cloud front; ■■■: numerical shock front with 50 μm particles; . . . . . .: numerical 50 μm particle cloud front; thin dashed line: numerical explosion products fronts for 50–100 μm particles merged at about 0.65 m

When the particle diameter is reduced, the acceleration of the particles becomes more sensitive to the drag acting on the particles. In other words, the momentum relaxation time scale between the two phases is reduced rapidly when the particle size is reduced. Thus, upon crossing the shock front, the particles are decelerated due to the drag from the air ahead of the shock. This is demonstrated in Fig. 11 with particles of 100 μm in diameter. Further reduction of the particle diameter enhances the particle deceleration, thus effectively dragging the particle front back to the shock front as shown in Fig. 11 for a particle diameter of 50 μm. Consequently, there exists a limit of the particle diameter, below which the time scale for the momentum relaxation between the two phases is so small that the velocity of the particles quickly matches the gas velocity. In this case, when the particles reach and penetrate the shock front, they decelerate and subsequently travel in close proximity with the shock front.

Another important parameter determining the particle inertia is the material density of the particles. From the momentum equation of the solid flow (15), the acceleration of the particle cloud depends on the particle material density with the leading order of $O(1/\rho_s)$ in the pressure gradient of the solid flow and the drag, in which the momentum relaxation time scale is proportional to the particle material density. A reduction of the particle material density causes an increase in the particle acceleration in the early dispersal stage which therefore reduces the overtaking distance. The influence of the particle material density on the overtaking distance is displayed in Fig. 12 for a spherical charge diameter of 11.8 cm and a particle diameter of 463 μm. The overtaking distance is reduced by a factor between 2.5 and 3 when steel particles are replaced by glass particles with the same diameter. Considering the material density of 7.8 g/cm^3 for steel particles and 2.7 g/cm^3 used for glass particles, the overtaking distance is approximately proportional to the material density of solid particles. Note that although experimental data for the blast wave trajectory is available with charges containing glass particles, the particles were not visible on the radiographs, so no data is available on the glass particle trajectory.

4.4 Effects of solid volume fraction

When the particle concentration or solid volume fraction is reduced, less momentum loss takes place from the gas to the particles during the charge detonation and the early propagation of the blast wave. Consequently, more momentum stored in the gas is available to drive fewer particles. The gain of this driving impulse causes an increase of the particle acceleration in the early dispersal stage. Figure 13 shows a comparison of the trajectories computed with the model for particle volume fractions of 62% and 30% for an 11.8 cm spherical charge filled with steel particles of 463 μm. A reduction of the particle volume fraction from 62% to 30% results in a smaller deficit of the shock

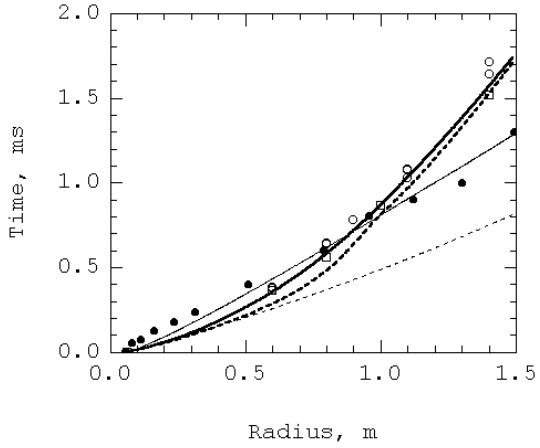

Fig. 12. Influence of particle material density on trajectories. The spherical charge is 11.8 μm in diameter and consists of a packed bed of 463 μm particles saturated with sensitized nitromethane. ○: Experimental shock front with steel particles; ●: experimental front of steel particle cloud; □: experimental shock front with glass particles; thick line: numerical shock front with steel particles; thin line: numerical steel particle cloud front; ■■■: numerical shock front with glass particles; . . .. . .: numerical glass particle cloud front

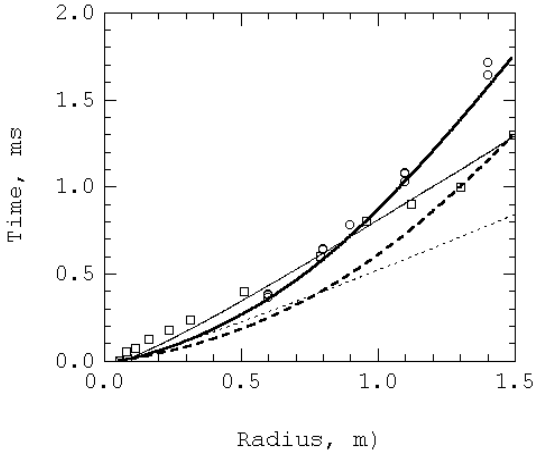

Fig. 13. Influence of particle volume fraction on trajectories. The spherical charge is 11.8 μm in diameter and consists of packed beds of 463 μm particles saturated with sensitized nitromethane. ○: Experimental shock front for a solid volume fraction of 0.62; □: experimental particle cloud front with a volume fraction of 0.62; thick line: numerical shock front for a solid volume fraction of 0.62; thin line: numerical particle cloud front with a volume fraction of 0.62; ■■■: numerical shock front for a solid volume fraction of 0.3; . . .. . .: numerical particle cloud front with a volume fraction of 0.3

velocity and a reduction of the predicted overtaking distance by a factor of 1.2. No experiments were carried out with a reduced volume fraction of solid particles due to the difficulties in uniformly suspending the particles in the nitromethane. To suspend the particles, it is necessary to add a substantial amount of gelling agent (e.g., PMMA) to nitromethane, which will change the detonation properties of the explosive.

5 Conclusions

This study has investigated the dispersal of inert solid particles by the detonation of a spherical explosive charge containing a packed bed of solid particles. The results of this experimental and numerical investigation indicate that, when the detonation reaches the surface, the frontal particles rapidly accelerate within a distance on the order of the charge diameter to a terminal velocity. Once accelerated, the particle velocity is roughly constant and the inertia of the particles allows them to penetrate through the combustion products and to overtake the decelerating, diverging primary shock front. The dominant driving forces for the particle acceleration can be attributed to the expansion of the combustion products through the drag, and to the large pressure gradient generated at the front of the packed bed of particles when the detonation reaches the charge surface. For a cylindrical charge geometry, particles may also overtake the primary shock front. However, for a planar charge geometry, it is unlikely that the particles will overtake the shock front due to the weak deceleration of the shock front.

The distance required for the frontal particles to overtake the shock front strongly depends on the charge size or mass and the material density of the particles, but weakly depends on the solid volume fraction. For the spherical charge geometry, a correlation for the overtaking distance, R_O, can be approximately written as:

$$R_O \sim \rho_s d \sim \rho_s m^{1/3} \tag{28}$$

where the parameter d is the charge diameter, ρ_s is the material density of solid particles and m denotes the charge mass. Concerning the particle size, there exists a particle size limit above which the distance required for the particles to overtake the shock front is not very sensitive to the particle size. Below this limit, the overtaking distance depends on the particle size. However, when the particles are sufficiently small, they cannot overtake the shock front.

Acknowledgements. The authors wish to acknowledge the invaluable assistance of T. Storrie, K. Gerrard, A. Nickel, L. Beaupre, and the DRES instrumentation and photo groups during the trial series.

References

Baer MR, Nunziato JW (1986) A two-phase mixture theory for the deflagration-to-detonation transition (DDT) in reactive granular materials. Int. J. Multiphase Flow 12:861

Baer MR (1997) Shock wave structure in heterogeneous reactive media. In: Houwing et al. (eds) Proceedings of the 21st International Symposium on Shock Waves, pp. 923–927

Colella P, Glaz HM (1985) Efficient solution algorithms for the Riemann problem for real gases. J. Comp. Phys. 59:264–289

Embid F, Baer M (1992) Mathematical analysis of a two-phase continuum mixture theory. Continuum Mech. Thermodyn. 4:279–312

Fried LE, Howard WM, Souers PC (1998) Cheetah 2.0 User's Manual. Energetic Materials Center, Lawrence Livermore National Laboratory

Frost DL, Kleine H, Slanik M, Higgins A, McCahan S, Zhang F, Murray SB (1999) Blast waves from heterogeneous explosives. Proceedings of the 22nd International Symposium on Shock Waves

Kurbangalina RKh (1969) Critical diameter of liquid explosives as a function of powder content. Zhurnal Prikladnoi Mekhaniki I Tekhnicheskoi Fiziki 10(4):133–136

Lanovets VS, Levich VA, Rogov NK, Tunik Yu-V, Shamshev KN (1991) Dispersion of the detonation products of a condensed explosive with solid inclusions. Fizika Goreniya i Vzryva 29:88–92

Lee JJ, Frost DL, Lee JHS, Dremin A (1995a) Propagation of nitromethane detonation in porous media. Shock Waves 5:115–119

Lee JJ, Brouillette M, Frost DL, Lee, JHS (1995b) Effect of diethylenetriamine sensitization on detonation of nitromethane in porous media. Combustion and Flame, 100:292

Powers, JM, Stewart, DS, Krier H (1990) Theory of two-phase detonation. Combustion and Flame 80:264–279

Rudinger G (1980) Fundamentals of gas-particle flow. Elsevier Scientific Publishing, New York

Sheffield SA, Hayes DB, Mitchell DE (1977) An equation of state and chemical kinetics for hexanitrostilbene (HNS) explosive. 6th Symposium (International) on Detonation, pp. 748–754

Zhang F, Tran D, Thibault PA (1996) Multiphase models for detonations and explosions in a dusty or porous medium. Combustion Canada '96, Ottawa

Zhang F, Thibault PA, Frost DL, Murray SB (1997) Explosive dispersal of solid particles. 15th International Symposium on Military Aspects of Blast and Shock, Banff, AB, Canada.

Zhang F, Murray SB, Frost DL, Thibault PA (1999) Some fundamental problems in blast modeling of solid particle-explosive charges. International Workshop on the Modeling of Non-Ideal Explosives, Socorro, NM.